International Journal of Chemical Studies

P-ISSN: 2349–8528
E-ISSN: 2321–4902
www.chemijournal.com
IJCS 2021; 9(2): 59-68

Received: 15-01-2021
Accepted: 20-02-2021

Pushpendra S Jaget
Department of P.G. Studies and Research in Chemistry and Pharmacy, Rani Durgavati Vishwavidyalaya, Jabalpur, Madhya Pradesh, India

Pradeep K Vishwakarma
Department of P.G. Studies and Research in Chemistry and Pharmacy, Rani Durgavati Vishwavidyalaya, Jabalpur, Madhya Pradesh, India

Mahendra K Parte
Department of P.G. Studies and Research in Chemistry and Pharmacy, Rani Durgavati Vishwavidyalaya, Jabalpur, Madhya Pradesh, India

Ram C Maurya
Department of P.G. Studies and Research in Chemistry and Pharmacy, Rani Durgavati Vishwavidyalaya, Jabalpur, Madhya Pradesh, India

Corresponding Author:
Pradeep K Vishwakarma
Department of P.G. Studies and Research in Chemistry and Pharmacy, Rani Durgavati Vishwavidyalaya, Jabalpur, Madhya Pradesh, India

A Ru (II) complex of 2-(diphenylphosphino)-benzylidene and ethanethiol, cis-[RuCl2 (P-N) (PPh3) (EtSH)]: A computational approach

Pushpendra S Jaget, Pradeep K Vishwakarma, Mahendra K Parte and Ram C Maurya

Abstract
This manuscript reports the computational studies of a previously synthesised compound, *cis*-[Ru Cl_2 (P-N) (PPh_3) (EtSH)] **1.** The optimised molecular structure, orbital and atomic charge analysis, NLO assets and electrostatic potential properties were studied through DFT approaches via mixed basis set at B3LYP/LANL2DZ level of theory. Therefore, the computed ^{1}H and ^{13}C-NMR chemical shifts were obtained with the GIAO method. Moreover, the TD-DFT based electronic absorption spectrum was computed using the PCM model. The theoretical studies were used to explain the molecular structures of the studied compound. Finally, insilco ADME properties were studies show good physiochemical and bioactivity of the studied compound.

Keywords: Ru (II) complex, FMOs, NLO, TD-DFT and ADME

Introduction
The discovery of NO, CO, and H_2S as small signalling gasotransmitters has developed a new type of science that endogenously derived gases could elicit crucial biological functions and contribute to the pathogenesis of human diseases (Hermann. 2012) [15]. In mammals, H_2S is endogenously produced by enzymatic reactions, even if some non-enzymatic pathways are involved in the biochemistry of hydrogen sulphide. It is present in micro molar concentrations in blood (Zhao *et al.*, 2001) [38]. Manifold chemical and biochemical catabolic fates await newly synthesised H_2S, and many more are probably still to be discovered (Li *et al.*, 2011) [21]. Despite these biochemical means for H_2S catabolism, it is a powerful reducing agent and is likely to be consumed by endogenous oxidant species in the vasculature (Whiteman *et al.*, 2004; Chang *et al.*, 2008; Geng *al*, 2004) [37, 6, 13], *viz*., peroxynitrite, superoxide and hydrogen peroxide. According to another report (Bayse *et al.*, 2013) [2] H_2S being a weak acid (pK_{a1}:6.76, pK_{a2}: 19.6) exists primarily as SH^- (82%) rather than H_2S (18%) or S_2^- (< 0.1%) under physiological conditions. It should be emphasised that H_2S and SH^- may both contribute directly to the biological action of hydrogen sulphide, and that SH^-, the predominant sulphide species under physiological conditions, is a more potent nucleophilic than Cys or reduced glutathione (GSH), which readily binds to metal centres in biological molecules (e.g., haemoglobin) or reacts with other compounds. The second pKa value (pKa_2) of H_2S is now settled (Hughes *et al.*, 2009) [17] to be 19±2. Therefore, the sulphide anion S^{2-} is present at low concentrations at pH 7.4, with a mole fraction of 1.7×10^{-12} and is unlikely to participate in the biological chemistry of H_2S. Hydrogen sulphide is rapidly oxidised, mainly in mitochondria, initially to thiosulfate and subsequently to sulphite and sulphate. This oxidation is not enzymatically driven, while thiosulfate conversion to sulphate or sulphite is catalysed by thiosulfate cyanide sulfotransferase (TST). Also, sulphite originating through this reaction is quickly oxidised to sulphate, as sulphate is the major end-product of H_2S metabolism under physiological conditions. However, urinary thiosulfate is considered a nonspecific marker of whole-body H_2S production (Belardinelli *et al.*, 2001) [5]. H_2S is soluble in many solvents, including water, acetone, carbon disulphide, methanol, ethanol, ether, chloroform, and benzene. Some data on the solubility of H_2S in a range of non-aqueous solvents are available (Fischer *et al.*, 2002; Guenther *et al.*, 2001) [10, 14]. At concentrations of <100 ppm, the toxic effects of H_2S in humans include eye irritation, sore throat, dizziness, nausea, shortness of breath, and chest tightness (Beauchamp *et al.*, 1984; Reiffenstein *et al.*, 1992) [3, 33].

Exposure to hydrogen sulphide at >1000 ppm concentration may cause severe adverse effects, especially for the central nervous system (CNS) and respiratory depression, ranging from loss of consciousness to death. The primary cause of death from H_2S poisoning has been attributed to respiratory paralysis (Kage *et al.*, 2002; Humbert *et al.*, 1990; Stone *et al.*, 1995) [19, 18, 35].

In the ongoing modern research, many reports have been published on the computational calculations manifested through density functional theory (DFT). DFT is a suitable technique to provide insights into the species' properties that arises in metal-organic frameworks. Theoretical chemistry plays a vital role in explaining the fundamental properties and communicating vast information about the physical and chemical properties of the molecule. It has been used to predict and establish the structural and spectral properties, surface analysis, molecular orbital and charges analysis of the micro and macromolecules (Mir *et al.*, 2017; Mir *et al.*, 2018; Meftah *et al.*, 2021; Parte *et al.*, 2021; Anil Kumar *et al.*, 2021; Bedoura *et al.*, 2022) [24, 25, 23, 28, 1, 3]. The frontier molecular orbitals (FMOs) and the simulated electronic absorption spectrum may also be determined by the TD-DFT method as is implemented in the Gaussian 09 program (Frisch *et al.*, 2010) [11]. DFT and TD-DFT calculations were performed thoroughly to obtain better insight into the electronic structures of the complexes and to correlate experimental and theoretical interpretation (Patra *et al.*, 2020) [29]. DFT meets the requirements of being accurate, easy to use, and fast enough to study relatively large molecules of transition metal complexes.

Experimental

Computational methodology: The computational calculations in this work were performed by Gaussian 09 programme (Frisch *et al.*, 2010) [11]. The studied compound *cis*-[$RuCl_2$ (P-N) (PPh_3) (EtSH)] 1 (Erin *et al.*, 2012) [9], was optimised at B3LYP/LANL2DZ level of theory. All the computations were done in the gaseous state to find the minimal energy at the maximum state of instability. The vibrational frequencies of the studied molecule the corresponding normal modes were evaluated at the optimised geometry using the same basis sets. Gauss View 05 animation programme (Dennington *et al.*, 2009) [7] help to visualisation of vibrational modes. The main motive for selecting the LANL2DZ basis set is its relativistic effect essential for heavy elements like metal complexes. The insilco ADME properties, including four parameters like absorption, distribution, metabolism, and excretion, were predicted with the support of the Swiss ADME web tool (Zoete *et al.*, 2016) [39]. The graphical output of the programme, namely the bioavailability radar, has been utilised for the prediction of significant physicochemical parameters which determine the preliminary appropriateness of the lead molecule for drug development.

Result and Discussions

Molecular Structural Framework: The optimised molecular structure of the studied compound *cis*-[$RuCl_2$ (P-N) (PPh_3) (EtSH)] is shown in Figure 1. The selected geometrical parameters, namely desired interatomic distances (Å) and angles (°), are tabulated in Table 1. In compound **1**, the Ru(II) centre is octahedrally surrounded by six donor atoms of five ligands, and primarily two chlorine atoms are coordinated as *cis* position, which is different from 90◦ Cl(3)-Ru-Cl(4), 94.300. The distance of Ru-Cl (3) 2.523 Å is longer than the bond length of another chlorine atom presented in the same molecule, Ru–Cl (4) 2.509 Å. This is expected due to the trans strengthening effect of the C_2H_5SH group. The third-fourth coordination by nitrogen and phosphorus donor atoms of the P-N ligand, forming six-membered chelate ring around RuN5C12C9C10P63 with a bite angle of N(5)-Ru-P(63) 87.608. The fifth position is occupied by phosphorus atom, Ru–P distances observed is 2.425 Å are comparable with those of other ruthenium complexes (Mosaferi *et al.*, 2016; Raynaud *et al.*, 2020) [26, 32]. Finally, the sixth position is occupied by the sulphur donor atom of the C_2H_5SH molecule. In such examples, the ruthenium centre approximately linearly with three transpositions, which is different from 180◦ [S (2)-Ru-Cl (4); 174.550°, Cl (3)-Ru-N (5), 176.042◦ and P (29)-Ru-P (63); 165.968°].

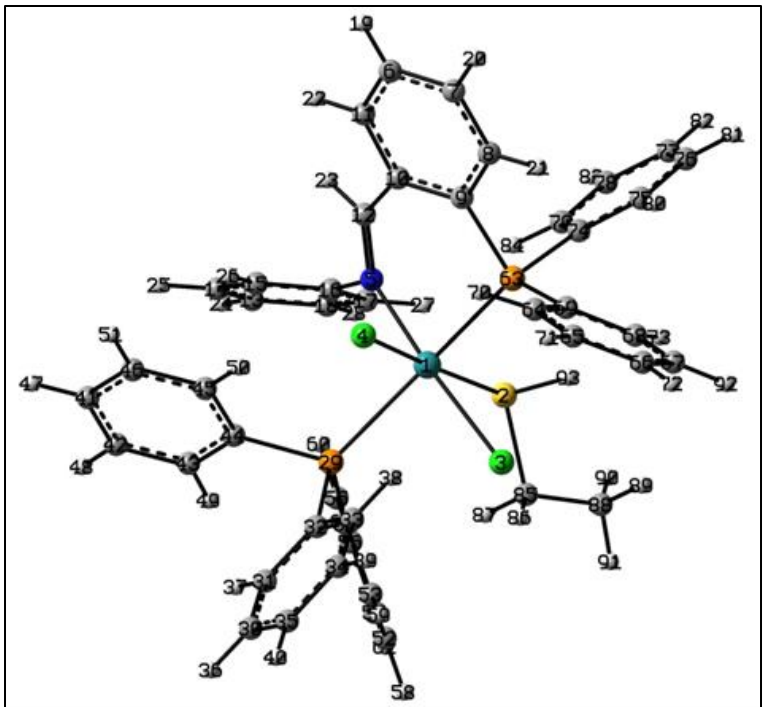

Fig 1: Selected optimized geometrical parameters of *cis*-[$RuCl_2$ (P-N) (PPh_3) (EtSH)] 1

Table 1: Selected optimized geometrical parameters of *cis*-[$RuCl_2$ (P-N) (PPh_3) (EtSH)] 1

Bond Connectivity	Bond Length (Å)	Bond Connectivity	Bond Angle (◦)	Bond Connectivity	Bond Angle (◦)
Ru-S(2)	2.583	S(2)- Ru- Cl(3)	81.954	Cl(3)- Ru- P(63)	88.952
Ru-Cl(3)	2.523	S(2)- Ru- Cl(4)	174.550	Cl(4)- Ru- N(5)	87.246
Ru-Cl(4)	2.509	S(2)- Ru- N(5)	96.244	Cl(4)- Ru- P(29)	84.354
Ru-N(5)	2.114	S(2)- Ru- P(29)	99.217	Cl(4)- Ru- P(63)	83.341
Ru-P(29)	2.425	S(2)- Ru- P(63)	92.602	N(5)- Ru- P(29)	98.518
Ru-P(63)	2.423	Cl(3)- Ru- Cl(4)	94.300	N(5)- Ru- P(63)	87.608
S(2)-C(85)	1.920	Cl(3)- Ru- N(5)	176.042	P(29)- Ru- P(63)	165.968
N(5)-C(12)	1.321	Cl(3)- Ru- P(29)	85.269	Ru(1)-N(5)-C(12)	127.004
				Ru(1)-S(2)-C(85)	114.700

Vibrational Spectral Studies: The IR spectrum of the studied compound *cis*-[$RuCl_2$ (P-N) (PPh_3) (EtSH)] 1 was theoretically computed with the Gaussian 09 programme. The molecular geometry optimisation of the compound formed no imaginary frequencies on the vibrational spectrum confirms that the shape assumed corresponds to minima on their potential energy surface. The computed infrared spectrum is displayed in Figure 2**.** The significant peaks are observed in the higher wavelength (cm^{-1}) region at 3278-3213 for *ν*(Ar-H, aryl group), 3130 *ν*(C-H, methylene group) and 3038 for stretching vibration of *ν*(C-H, methyl group). Therefore, the four characteristic peaks appeared in the mid-IR region at 1628, 1583, 1460 for *ν*(C=C) and strong band at 1515 cm^{-1} *ν*(C=N). Moreover, some characteristics peaks appeared in lower wavelength (cm^{-1}) reign at 728; *ν*(C-S), 531; *ν*(Ru-N), 493, 462; *ν*(Ru-Cl), 352; *ν*(Ru-S) and 280, 220 are assigned *ν*(Ru-P), it provides an essential explanation for the metal-ligand bonding. Finally, the single peak observed at 2516 cm^{-1} is given stretching vibration of *ν*(S-H). The animation program of Gauss View 05 was used to enlighten the functional group assignments.

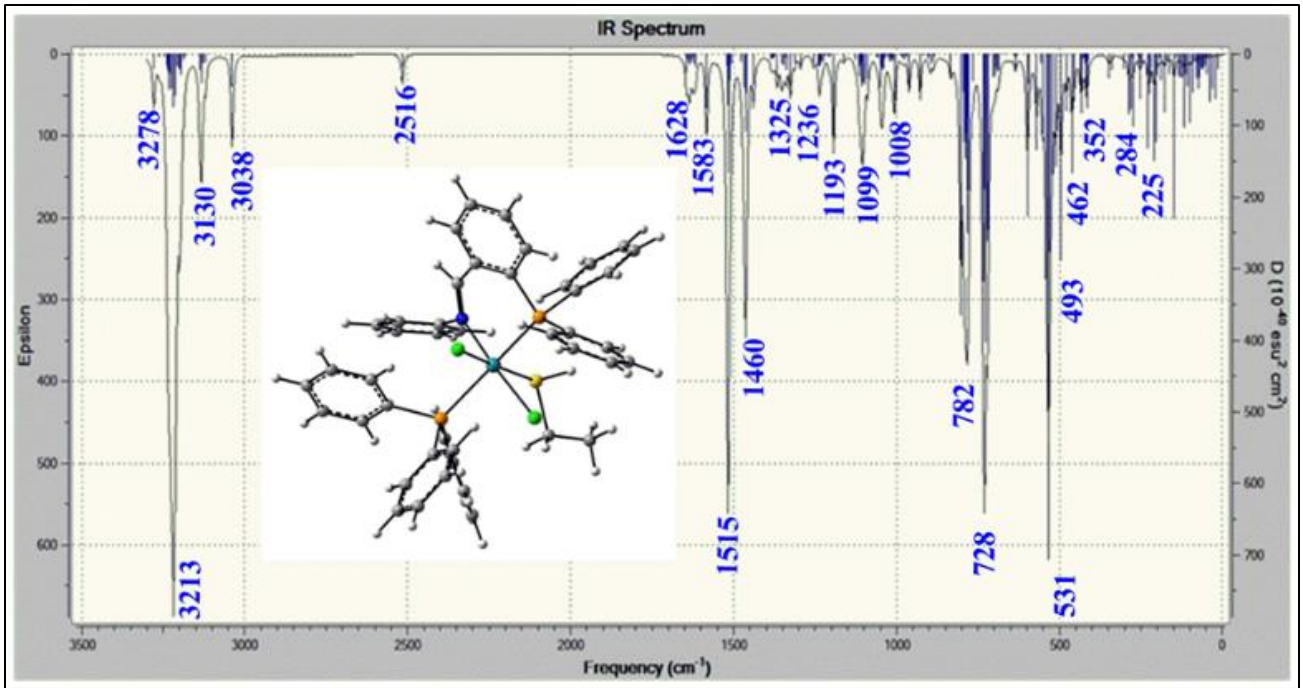

Fig 2: vibrational infrared spectrum of *cis*-[$RuCl_2$ (P-N) (PPh_3) (EtSH)] 1

NMR Spectral Studies: The ^1H and ^{13}C-NMR chemical shifts δ (ppm) was computed with the gauge independent atomic orbital (GIAO) method and tetramethylsilane (TMS) was used as reference material with the DFT approach. The computed ^1H-NMR chemical shift δ (ppm) are shown in Figure 3, and their assignment are summarised in Table 2. The multiple chemical shifts at 6.42- 7.50 δ (ppm) have been assigned to the eighteen aromatic protons of P-N ligand moiety. Other peaks observed in the region at 6.42- 7.50 δ (ppm) are given to the fifteen aromatic protons of PPh_3 ligand moiety. Moreover, a single peak was monitored at 8.18 δ (ppm) has been attributed to the (-HC=N) proton of the Schiff base ligand moiety. The two singlet proton peaks were observed at 2.73, and -1.34 ppm are assigned as aliphatic proton of (CH_2) ethanethiol. The three singlet proton peaks were observed at -0.48, -0.14 and 0.11 ppm are assigned as aliphatic proton of methyl (CH_3) group of ethanethiol. Finally, a single peak was observed at 0.16 δ (ppm) has been attributed to the (-SH) proton of ethanethiol moiety.

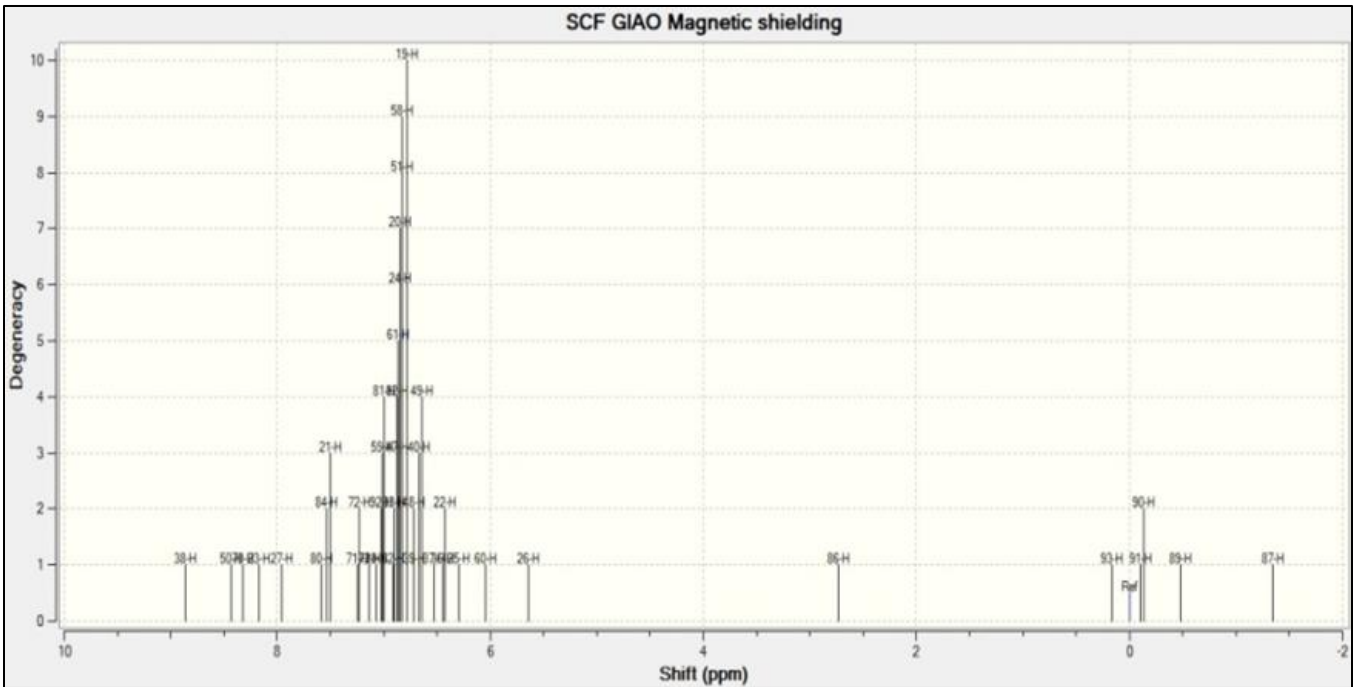

Fig 3: ^{1}H-NMR spectrum of *cis*-[$RuCl_2$ (P-N) (PPh_3) (EtSH)] 1

The six-coordinate compound *cis*-[$RuCl_2$ (P-N) (PPh_3) (EtSH)] 1 with five ligands show forty-seven ^{13}C signals. The ^{13}C chemical Shift (ppm) and their assignment are presented in Table 3. Only three ligands show carbon signals out of the five, while two identical chlorine ligands do not show any chemical shift. The first ligand, P-N donor Schiff base show twenty-four ^{13}C signals of aromatic carbon around 117.88-156.89 δ (ppm). The second large number of ^{13}C signals show from 119.10-144.21 δ (ppm) attributed to aromatic carbons of the PPh_3 ligand. Finally, the ethanethiol ligand shows only three ^{13}C signals at 176.37, 27.99, and 11.61 δ(ppm) has been attributed to the amine carbon of P-N ligand (-HC=N), carbon of methylene (CH_2) group and carbon of methyl (CH_3) group, respectively.

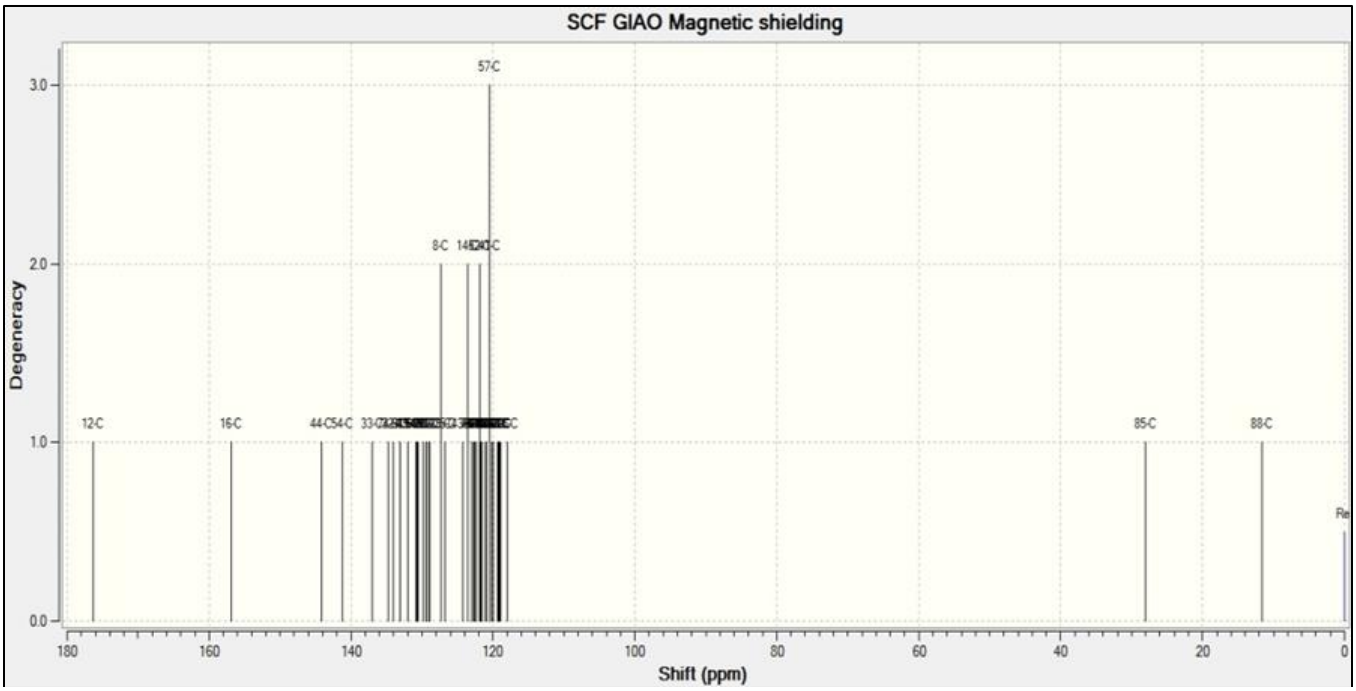

Fig 4: ^{13}C-NMR spectrum of *cis*-[$RuCl_2$ (P-N) (PPh_3) (EtSH)] 1

Table 2: Theoretical chemical shift values of ^{1}H-NMR and their assignment

Atom	Chemical Shift (ppm)		Atom	Chemical Shift (ppm)	Assignment
H(19)	6.82	Aromatic proton of P-N ligand	H(24)	6.85	The aromatic proton of PPh3
H(20)	6.85		H(25)	6.29	
H(21)	7.50		H(26)	5.64	
H(22)	6.42		H(27)	7.95	
H(58)	6.83		H(28)	7.07	
H(59)	7.01		H (36)	6.44	
H(60)	6.04		H(37)	6.53	
H(61)	6.86		H(38)	8.86	
H(62)	6.90		H(39)	6.71	
H(70)	8.31				
H(71)	7.24		H(40)	6.67	
H(72)	7.22		H(47)	6.88	
H(73)	7.14		H(48)	6.71	
H(80)	7.58		H(49)	6.63	
H(81)	6.11		H(50)	8.43	
H(82)	6.87		H(51)	6.83	
H(83)	6.90		H(86)	2.73	The proton of methylene (CH_2) group of ethanethiol
H(84)	7.53		H(87)	-1.34	
H(92)	7.02		H(89)	-0.48	Proton of methyl (CH_3) group of ethanethiol
H(23)	8.18	Amine proton of P-N ligand	H(90)	-0.14	
H(93)	0.16	The proton of (SH) ethanethiol	H(91)	-0.11	

Table 3: Theoretical chemical shift values of 13C NMR and their assignment

Atom	Chemical Shift (ppm)	Assignment	Atom	Chemical Shift (ppm)	Assignment
C(6)	122.32	Aromatic carbon of P-N ligand	C(12)	176.37	Amine carbon of P-N ligand
C(7)	123.61		C(30)	119.10	Aromatic carbon of PPh3
C(8)	127.29		C(31)	129.49	
C(9)	133.03		C(32)	134.09	
C(10)	128.82		C(33)	136.98	
C(11)	132.00		C(34)	119.95	
C(13)	119.19		C(35)	121.22	
C(14)	123.57		C(41)	120.44	
C(15)	117.88		C(42)	120.51	
C(16)	156.89		C(43)	124.30	
C(17)	119.31		C(44)	144.21	
C(18)	120.94		C(45)	131.94	
C(64)	130.82		C(44)	144.21	
C(65)	121.81		C(45)	131.94	
C(66)	122.51		C(46)	121.71	
C(67)	118.93		C(52)	121.81	
C(68)	130.55		C(53)	130.72	
C(69)	129.89		C(54)	141.27	
C(74)	134.82		C(55)	129.09	
C(75)	126.71		C(56)	120.24	
C(76)	123.00		C(57)	120.47	
C(77)	122.75		C(85)	27.99	Methylene (CH_2) of ethanethiol
C(78)	121.57		C(88)	11.61	Corban of Methyl (CH_3) of ethanethiol
C(79)	127.29				

Electronic Absorption Spectral Studies: The UV-Vis absorption spectrum of the studied compound 1 was computed using the PCM model's time-dependent density functional theory (TD-DFT) method. The first maxima (λmax) were detected at 528 nm with three excitations between HOMO-2 to LUMO, HOMO-1 to LUMO and HOMO to LUMO. The second (λmax) was observed at 598 nm with two excitations between HOMO-2 to LUMO and HOMO to LUMO. Finally, the third (λmax) was observed at 606 nm with five excitations between HOMO to LUMO, HOMO to LUMO+1, HOMO to LUMO+2, HOMO to LUMO+3 and HOMO to LUMO+9. The overall 558 molecular orbitals involved the electronic density distributions and electronic excitations from lowest to the higher energy transition, which are orbital number 182 is meant for HOMO and 183 for LUMO. The acronyms stand for the highest occupied molecular orbital (HOMO), lowest unoccupied molecular orbital (LUMO). The FMOs analysis plays a dynamic role in understanding the complexation behaviour and determining a conjugate system's reactive position. It also determines the physical and chemical parameters like kinetic stability, molecular reactivity, chemical potential, optical polarizability, softness-hardness, and electrophilicity of the molecules (Fukui, 1982; Pearson, 1993) [30,12]. In connection herein, the six selected FMOs and their energy gap are calculated directly. The difference in the $E_{HOMO-LUMO}$ value is presented in Figure 5, and data are plotted in Table 4. The compound observed E_{HOMO} -4.84 and E_{LUMO} -2.03 eV, and its energy gap ΔE is 2.81 eV; The red and green colours contour indicates the positive and negative values for the wave function. Compound **1** exhibited E_{HOMO-2}, E_{HOMO-1}, and E_{HOMO+1} were mostly localised on the metal

centre. However, the E_{LUMO+1} and E_{LUMO+2} are concentrated over the entire molecule. But, the E_{LUMO} is focussed on the whole molecule, excluding the aromatic ring of PPh_3. Moreover, for a clear understanding of FMO's, some applied quantum chemical parameters like electronegativity (χ), global hardness (η) and global softness (S), were determined and given in Table 4.

Table 4: Theoretical electronic absorption spectral values of *cis*-[$RuCl_2$ (P-N) (PPh_3) (EtSH)] 1 and their assignment oscillator strength along with major contribution (%).

λmax nm	eV	Oscillator strength (f) fosc (× 10^{-4})	Major Contribution (%)	Peak Assignment	Quantum chemical parameters	
					Parameters	Value
606	2.046	34.0	HL(30)	MLCT	HOMO	-4.84
			H→ L+1(31)		LUMO	-2.03
			H→ L+2 (29)		ΔE(HOMO-LUMO)	2.81
			H→ L+3(25)		Electronegativity (χ)	1.40
			H→ L+9(11)		Global hardness (η)	-3.43
598	2.074	96.0	H-2→L (11)	LMCT	Global softness (S)	-0.29
			HL(44)			
528	2.347	216.0	H-2→L(43)	ILCT		
			H-1→ L(35)			
			HL(21)			

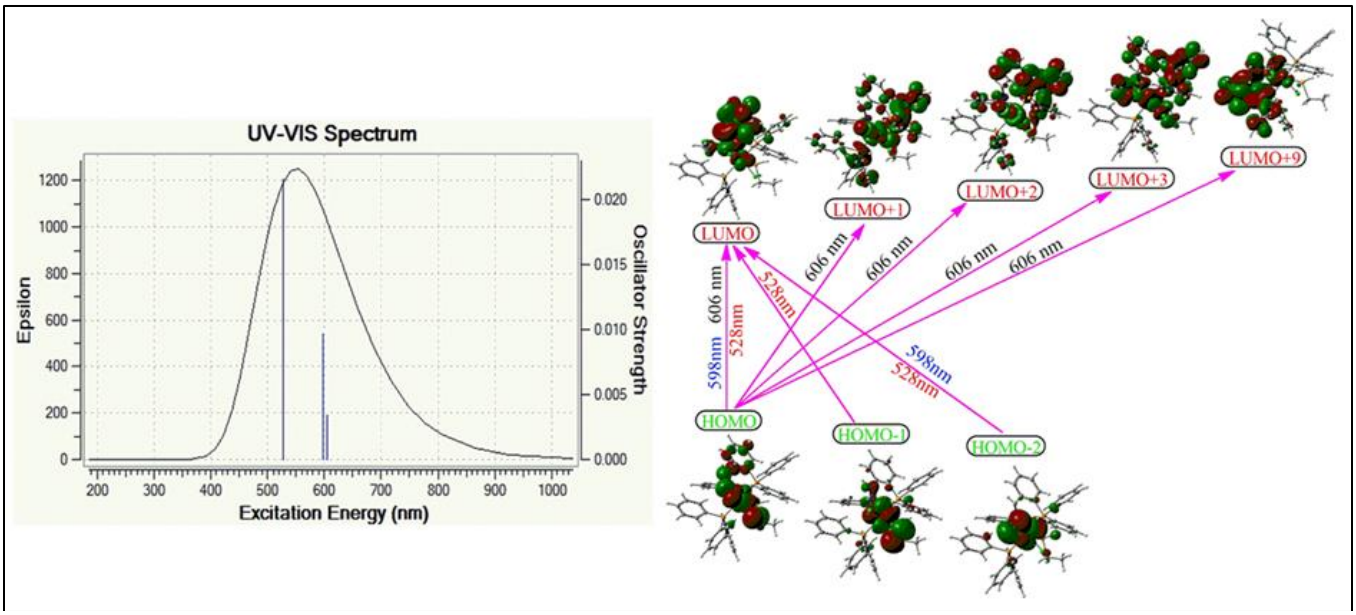

Fig 5: Electronic absorption spectrum (left) and FMOs excitation (right) of *cis*-[$RuCl_2$ (P-N) (PPh_3) (EtSH)] 1

NLO Properties: NLO properties provide the key functions for optical materials like optical telecommunication, optical data storage, optical interconnects, integrated optics signal processing, and image reconstruction technologies of organic/inorganic materials and their potential applications. In the absence of experimental observations, theoretical chemistry plays a significant role in understanding the structural property relationship, assisting in designing active NLO materials. It is attributed that the highest values of the dipole moment, molecular polarizability, and hyperpolarizability are significant for the more active NLO properties. Therefore, the NLO properties were theoretically calculated based on the relations of x, y, z components (Maurya *et al*., 2015; Rahmani *et al*., 2018) [22, 31] as given by the following equations (i to v). This innovative molecular system's first hyperpolarizability (β_0) is calculated with the DFT technique based on the finite field approach. It is a third rank tensor 3 × 3 × 3 matrices can describe. The twenty-seven components of the 3D matrix can be reduced to ten components due to the Kleinman symmetry (Kleinman, 1962) [20] by following equation (v).

$$\mu = (\mu_x^2+\mu_y^2+\mu_z^2)^{1/2} \quad \text{... (i)}$$

$$\alpha = 1/3(\alpha_{xx}+\alpha_{yy}+\alpha_{zz}) \quad \text{… (ii)}$$

$$\Delta\alpha = \left[\frac{(\alpha_{XX}-\alpha_{YY})^2+(\alpha_{YY}-\alpha_{ZZ})^2+(\alpha_{ZZ}-\alpha_{XX})^2}{2}\right]^{1/2} \quad \text{... (iii)}$$

$$(\beta_0) = (\beta_x^2+\beta_y^2+\beta_z^2)^{1/2} \quad \text{···· (iv)}$$

and

$\beta_x = \beta_{xxx} + \beta_{xyy} + \beta_{xzz}$

$\beta_y = \beta_{yyy} + \beta_{xxy} + \beta_{yzz}$

$\beta_z = \beta_{zzz} + \beta_{xxz} + \beta_{yyz}$

or

$$(\beta_0) = [(\beta_{xxx}+\beta_{xyy}+\beta_{xzz})^2+(\beta_{yyy}+\beta_{yzz}+\beta_{yxx})^2+(\beta_{zzz}+\beta_{zxx}+\beta_{zyy})^2]^{1/2} \ldots (v)$$

In connection with herein calculated the NLO properties of the studied compound 1. The computed values about their tensor orders are summarised in Table 5. The values are as 6.813 D, -47.63×10^{-24}, 3.23×10^{-24}, and 9.61×10^{-31} esu. The polarizabilities and first-order hyperpolarizabilities are given in the atomic units (au), the calculated values have been converted into electrostatic units (esu) through the conversion

factor of 0.148×10^{-24} esu for α and 8.639×10^{-33} esu for β. In this study, Urea is selected as a reference as there were no experimental values of NLO properties of the studied compounds. The magnitude of the molecular hyperpolarizability β is one of the critical factors in the NLO system. Generally, highly efficient NLO materials are mainly consistent with noticeable charge transfer (CT) transitions.

Table 5: Dipole moment (μ), polarizability (α), Anisotropy of the polarizability (Δα) and Hyperpolarizability *(β)*

Dipole moment *(μ)*		**Hyperpolarizability *(β)***	
MX	1.435	β_{xxx}	89.303
μ_y	-6.088	β_{yyy}	38.824
μ_z	2.702	β_{zzz}	47.933
$\mu_{Tot.}$	6.813	β_{xyy}	-11.335
Polarizability *(α)*		β_{xxy}	2.077
α_{xx}	-308.545	β_{xxz}	26.754
α_{yy}	-333.661	β_{xzz}	17.237
α_{zz}	-323.236	β_{yzz}	-50.022
α_{xy}	8.003	β_{yyz}	-17.985
α_{xz}	-6.242	β_{xyz}	-16.225
α_{yz}	2.235	*β(0)*	9.61×10^{-31}
α	-47.63×10^{-24}		
Δα	3.23×10^{-24}		

Electrostatic potential: The molecular electrostatic potential (MEP), electrostatic potential (ESP), and total electron density (TED) of the studied compound are display in Figure 6. The TED plots define a unifying distribution of the electron density over the molecule. The applied approaches of MEP deceits in the fact that it simultaneously displays molecular shape and size. It's beneficial in molecular structure research with its physiochemical property relationship (Murray & Sen, 1996; Scrocco & Tomasi, 1978) [27, 34]. The MEP surface map is the electrostatics-oriented approach used to understand the site-specific reactive area over the molecule. MEP map predicts the molecules' reactivity, allows the visualisation of variable potential regions into molecules, and provides transparent information about the charge distribution. Electron distribution governs the MEP of the molecules. The diverse values of the electrostatic potential at the surface are represented via distinct colours. The potential increases from negative to positive charges in the order of red < orange < yellow < green < blue, which is related to the electrophilicity and nucleophilicity of the compounds. The MEP map shows that the maximum negative potentials region corresponds to the most electronegative atoms.

In contrast, the leading positive area corresponds to the most excellent electropositive atoms. Herein, the oxygen atoms of the sulfa drug moiety are more electronegative. At the same time, the maximum positive region is localised on hydrogen atoms, which correspond to the neutral groups. The remaining species are surrounded by zero potential. Such a variance in charge topography may result in the succeeding biological application of the Ru (II) compounds.

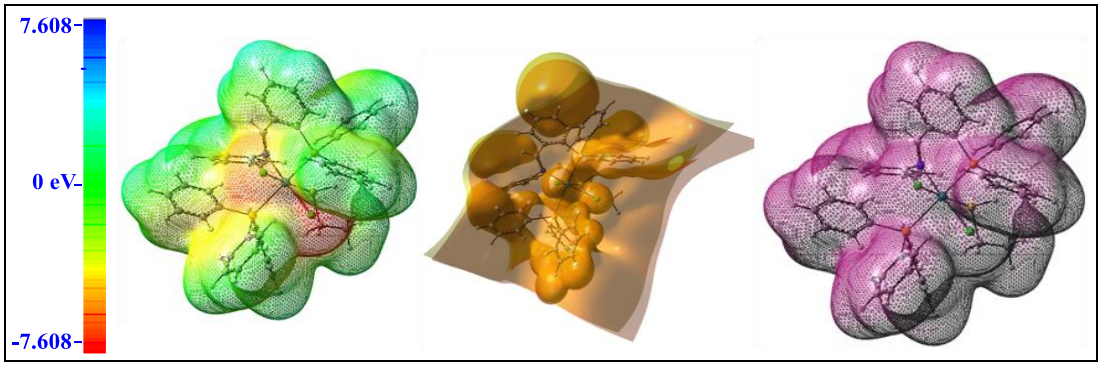

Fig 6: MESP, ESP and TED plots of compound *cis*-[$RuCl_2$ (P-N) (PPh_3) (EtSH)] 1

Charge analysis: The atomic charges of the studied compound **1** and it was obtained by Mulliken population analysis (Ebrahimi *et al.*, 2014) [8]. Mulliken atomic charge has played a vital role in applying quantum chemical calculations to molecular systems because atomic charges affect molecular structure properties, such as dipole moment and molecular polarizability. The compound's charge transfer shows high NLO activity due to delocalised electrons in the molecule (Heyd & Scuseria, 2004) [16]. The results show that the atoms in compound 1, namely hydrogens, bear positive charges, and the nitrogen is generally negatively charged inside the analyses. The carbon atoms bear positive and negative charges because they bind with nucleophilic and electrophilic atoms over the molecule. The ruthenium atom has the most significant negative charge (-0.257e) than the other atoms in evaluation. Because it is coordinated six atoms like, two phosphorus; P29(0.734e), P63(0.743e), two chlorine, Cl3(-0.334e), Cl4(-0.308e), one nitrogen N15(-0.247e), and finally one sulphur, S2(0.040e) they are negatively and positively charged atoms. Furthermore, Mulliken's atomic charges analysis confirms that ruthenium is basic due to the negatively charged atom; this is bind with two positively charged phosphorus atoms. The scale of the positive and negative charge of the atoms in the compound is shown in figure 7. The natural atomic charges computed by the Mulliken charge analysis of compound 1 is appended in Table 6.

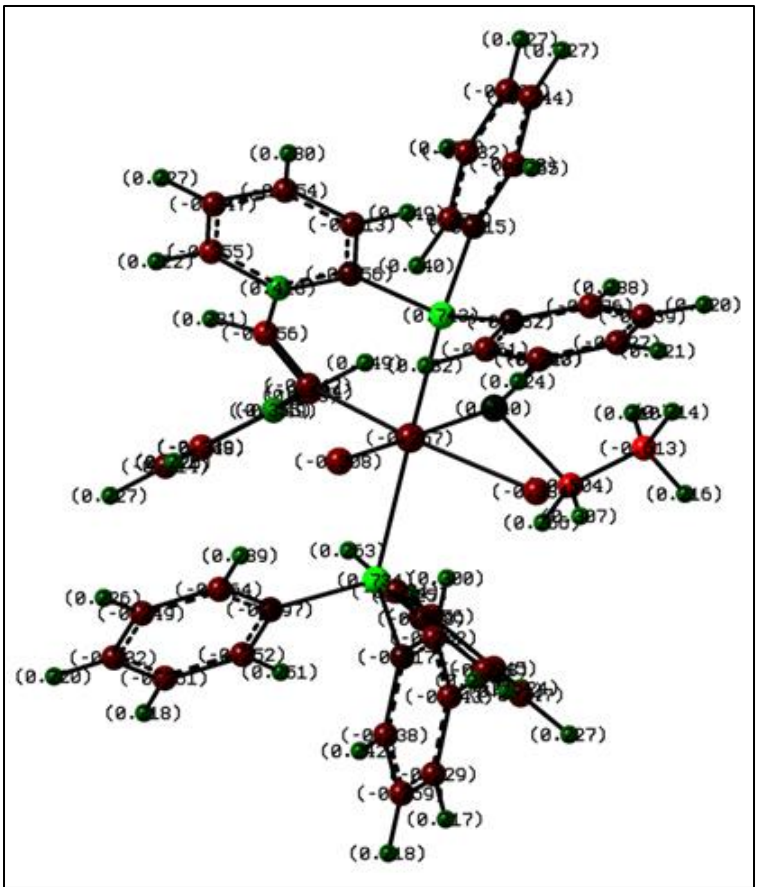

Fig 7: Mulliken atomic charge of *cis*-[$RuCl_2$ (P-N) (PPh_3) (EtSH)] 1 green colour (positive) and red (negative) charges

Table 6: Mulliken atomic charge of studied compound *cis*-[$RuCl_2$ (P-N) (PPh_3) (EtSH)] 1

Atoms	Charges	Atoms	Charges	Atoms	Charges	Atoms	Charges
Ru (1)	-0.257	H(25)	0.227	H(49)	0.251	H(73)	0.238
S(2)	0.040	H(26)	0.276	H(50)	0.289	C(74)	-0.115
Cl(3)	-0.334	H(27)	0.249	H(51)	0.226	C(75)	-0.273
Cl(4)	-0.308	H(28)	0.223	C(52)	-0.247	C(76)	-0.244
N(5)	-0.247	P(29)	0.734	C(53)	-0.248	C(77)	-0.231
C(6)	-0.247	C(30)	-0.259	C(54)	-0.128	C(78)	-0.232
C(7)	-0.254	C(31)	-0.238	C(55)	-0.274	C(79)	-0.274
C(8)	-0.213	C(32)	-0.117	C(56)	-0.256	H(80)	0.255
C(9)	-0.156	C(33)	-0.252	C(57)	-0.245	H(81)	0.227
C(10)	0.418	C(34)	-0.243	H(58)	0.227	H(82)	0.227
C(11)	-0.355	C(35)	-0.229	H(59)	0.271	H(83)	0.228
C(12)	-0.356	H (36)	0.218	H(60)	0.263	H(84)	0.240
C(13)	-0.248	H(37)	0.242	H(61)	0.225	C(85)	-0.504
C(14)	-0.214	H(38)	0.300	H(62)	0.224	H(86)	0.307
C(15)	-0.339	H(39)	0.224	P(63)	0.743	H(87)	0.267
C(16)	0.355	H(40)	0.217	C(64)	-0.261	C(88)	-0.613
C(17)	-0.304	C(41)	-0.232	C(65)	-0.240	H(89)	0.214
C(18)	-0.249	C(42)	-0.261	C(66)	-0.227	H(90)	0.210
H(19)	0.227	C(43)	-0.252	C(67)	-0.239	H(91)	0.216
H(20)	0.230	C(44)	-0.097	C(68)	-0.276	H(92)	0.220
H(21)	0.249	C(45)	-0.264	C(69)	-0.062	H(93)	0.123
H(22)	0.222	C(46)	-0.249	H(70)	0.282		
H(23)	0.231	H(47)	0.220	H(71)	0.224		
H(24)	0.226	H(48)	0.218	H(72)	0.221		

Insilco ADME Studies: The Swiss ADME predictor (http://www.swissadme.ch) assist to provide the insilco ADME properties, which displays good biological potential and oral administrative activities. The Swiss ADME predictor also offers additional information about the compound like molecular hydrophobicity (log P), topological polar surface area (TPSA) and bioavailability. According to Lipinski' rule, the log P values are detected to be less than five, representing a higher tendency to ease penetration to the cell membrane. TPSA is a very relevant physicochemical parameter, analysed by hydrogen bond, ability in the system which is used to predict the way of drug transport properties inside various parts of the body such as gastrointestinal tract, bioavailability, blood-brain barrier penetration. The metabolism is expected on the basis of five cytochrome phosphate (CYP) models, naming (CYP1A2, CYP2C19, CYP2C9, CYP2D6 and

CYP3A4) inhibitor along with one phosphatase glycoprotein (P-GP) substrate. These parameters were computed and verified for agreement with their standard ranges.

The insilco ADME properties of the studied compound *cis*-[$RuCl_2$ (P-N) (PPh_3) (EtSH)] 1 depicted in Table 7**.** The compound contains neither hydrogen bond donor (HBD) nor hydrogen bond acceptors (HBA). The compound contains nine rotatable bonds, revealing that they act as an oral administration mode: the TPSA value shows 78.34 Å² and a bioavailability score of 0.56. Therefore, the bioactive score is achieving more than zero, and they possess a higher probability and the biological activity of examined compound increases (Veber *et al*., 2002)[36]. The solubility score (log S) defines the soluble behaviour of the compound. It defines in the order of < -10; insoluble, < -6; poorly soluble, < -4; moderate soluble, < -2; soluble and < 0; highly soluble. In the current study, the log S score is -13.47. It is insoluble.

Table 7: Insilco ADME properties of studied compound *cis*-[$RuCl_2$ (P-N) (PPh_3) (EtSH)] 1

Physiochemical Parameters	1	Pharmacokinetic Parameters	1
Formula	$C_{45}H_{41}Cl_2NP_2RuS$	GI absorption	Low
Molecular weight	861.80 g/mol	BBB permeant	No
Num. heavy atoms	52	P-gp substrate	Yes
Num. arom. heavy atoms	42	CYP1A2 inhibitor	No
Fraction Csp3	0.04	CYP2C19 inhibitor	No
No. rotatable bonds	9	CYP2C9 inhibitor	No
No. H-bond acceptors	0	CYP2D6 inhibitor	No
No. H-bond donors	0	CYP3A4 inhibitor	No
Molar Refractivity	238.68	Log K_p (skin permeation)	-2.23 cm/s
TPSA	78.34 Å²	Bioavailability Score	0.56
Log P (Lipophilicity)	8.00	Synthetic accessibility	7.06
Log S (Solubility)	-13.47		

Conclusions

We have investigated in detail the computational studies of *cis*-[$RuCl_2$ (P-N) (PPh_3) (EtSH)] 1. To execute the geometry optimisations and frequency calculations at the B3LYP/LANL2DZ for the studies compound. The optimised molecular structure provides various geometrical parameters, namely bond lengths and bond angles, approving the six coordinated distorted octahedral geometry and calculating the global minimum energy E= - 974.80 Hartree of the studied compound. The IR vibrational intensity and their assignment display that the molecules' torsional and bending vibrations over there stretch. The order of the IR vibrations of the ruthenium-ligand bonds can be assumed as Ru-N > Ru-Cl > Ru-S > Ru-P. The theoretical NMR provides the 1H NMR, and 13C NMR chemical shift values are reported. Moreover, insilco ADME results are attributed to good pharmacokinetics and biological activity. The bioavailability score and TPSA value of studied compound 1 are 0.56 and 78.34 Å², respectively.

Declaration of Competing Interest

The authors declare that they have no known competing financial interests or personal relationships that could have influenced the work reported in this paper.

Acknowledgements

The authors are appreciated for acknowledging Professor Kapil Deo Mishra, Vice-Chancellor, Rani Durgavati Vishwavidyalaya, for their moral support and inspiration. We are also thankful to the Head of the Department for encouraging and providing facilities of the computational laboratory.

References

1. Anil Kumar S, Bhaskar BL. Preliminary investigation of drug impurities associated with the anti-influenza drug Favipiravir–An *in silico* approach. Comp. Theo. Chem 2021;1204:113375.
2. Bayse CA, Brumaghim JL. Eds. The Biological Chemistry of Sulfur, Selenium, and Tellurium. ACS Symposium Series; American Chemical Society: Washington. DC 2013. (Doi: http://dx.doi.org/10.1021/ic401366c).
3. Beauchamp Jr RO, Bus JS, Popp JA, Boreiko CJ, Andjelkovich DA. A Critical Review of the Literature on Hydrogen Sulfide Toxicity. Crit. Rev. Toxicol 1984;13:25-97.
4. Bedoura B, Xi HW, Goh HW, Lim KH. DFT/TDDFT Investigation on donor-acceptor triazole-based copolymers for organic photovoltaics J Mole. Struct 2022;1248:131406.
5. Belardinelli MC, Chablis A, Vekemans BC, Kamoun P. Urinary Sulfur Compounds in Down syndrome. Clin. Chem 2001;47:1500-1501.
6. Chang L, Geng B, Yu F, Zhao J, Jiang H, Du J *et al*. Hydrogen sulfide inhibits myocardial injury induced by homocysteine in rats. Amino Acids 2008;34:573-585.
7. Dennington R, Keith T, Millam J. Gauss View, Version 5, Semichem Inc., Shawnee Mission KS 2009.
8. Ebrahimi HP, Hadi JS, Abdulnabi ZA, Bolandnazar Z. Spectroscopic, thermal analysis and DFT computational studies of salen-type Schiff base complexes. Spectrochimica Acta A 2014;117:485-492.
9. Erin Ma SF, Steven Rettig J, Brian Patrick O, Brian James R. Ruthenium (II) Thiol and H2S Complexes: Synthesis, Characterization and Thermodynamic Properties. | Inorg. Chem 2012;51:5427-5434.
10. Fischer K, Chen J, Petri M, Gmehling J. Solubility of H_2S and CO_2 in N-octyl-2-pyrrolidone and of H_2S in methanol and benzene. AIChE Journal 2002;48:887-893.
11. Fukui K. Role of frontier orbitals in chemical reactions. Science 1982;218:747-754.
12. Gaussian 09, Revision B.01, Frisch MJ, Trucks GW, Schlegel HB, Scuseria GE *et al*. Gaussian, Inc., Wallingford CT 2010.
13. Geng B, Yang J, Qi Y, Zhao J, Pang Y. H_2S generated by heart in rat and its effects on cardiac function. Biochem. Biophys. Res. Commun 2004;313:362-368.
14. Guenther EA, Johnson KS, Coale KH. Direct Ultraviolet Spectrophotometric Determination of Total Sulfide and

Iodide in Natural Waters, Anal. Chem 2001;73:3481-3487.
15. Hermann A. Gasotransmitters: Physiology and Pathophysiology, Springer-Verlag Berlin Heidelberg 2012. Doi.org/10.1007/978-3-642-30338-8.
16. Heyd J, Scuseria GE. Assessment and validation of a screened Coulomb hybrid density functional. J Chem Phys 2004;120:7274-7280.
17. Hughes MN, Centelles NM, Moore KP. Making and working with hydrogen sulfide: The chemistry and generation of hydrogen sulfide *in vitro* and its measurement *in vivo*: A review. Free Radical Biology & Medicine 2009;47:1346-1353.
18. Humbert P, Niroomand F, Fischer G, Mayer B, Koesling D, Hinsch KD *et al*. Purification of soluble guanylyl cyclase from the bovine lung by a new immunoaffinity chromatographic method. Eur. J Biochem 1990;190:273-278.
19. Kage S, Kashimura S, Ikeda H, Kudo K, Ikeda N. Fatal and nonfatal poisoning by hydrogen sulfide at an industrial waste site. J Forensic Sci 2002;47:652.
20. Kleinman DA. Nonlinear dielectric polarization in optical media. Phys Rev 1962;126:1977.
21. Li L, Rose P, Moore PK. Hydrogen sulfide and cell signalling. Annu. Rev. Pharmacol. Toxicol 2011;51:169-187.
22. Maurya RC, Malik BA, Mir JM, Vishwakarma PK. Oxidovanadium(IV) complexes involving dehydroacetic acid and β-diketones of bioinorganic and medicinal relevance: Their synthesis, characterisation, thermal behavior and DFT aspects. J Mole. Struct 2015;1083:343-356.
23. Meftah Y, Boumedjane Y, Fleurat-Lessard P, Delbecq F, Michel C. Enantioselective reduction of prochiral ketones promoted by amino amide ruthenium complexes: A DFT study. J Organomet. Chemistry 2021;939:121765.
24. Mir JM, Jain N, Malik BM, Chourasia R, Vishwakarma PK, Rajak DK *et al*. Urinary tract infection-fighting potential of Newly synthesised ruthenium carbonyl complex of N-dehydroacetic acid-N'-o-vanillin-ethylenediamine. Inorg. Chim. Acta 2017;467:80-92.
25. Mir JM, Vishwakarma PK, Maurya RC. Conjoint experimental–theoretical evaluation of pyrone-salicylic acid hydrazide copper (II) Schiff base complexes: their synthesis, SOD and electrochemical fronts. J Chin. Adv. Mat. Society 2018;6:55-80.
26. Mosafer E, Pan L, Wang T, Sun Y, Pranckevicius C, Stephan DW. Preparation and reactivity of a Ru(0) phosphine–carbene complex. Dalton Trans 2016;45:1354-1358.
27. Murray JS, Sen K. Molecular Electrostatic Potentials. Concepts and 399 Applications. Elsevier, Amsterdam 1996.
28. Parte MK, Vishwakarma PK, Jaget PS, Maurya RC. Synthesis, spectral, FMOs and NLO properties based on DFT calculations of dioxidomolybdenum (VI) complex. J Coord. Chem 2021;74:584.
29. Patra VR, Maity A, Rajak KK. Synthesis, crystal structure, DFT calculation and trans→cis isomerisation studies of bipyridyl ruthenium (II) complexes bearing 8-oxyquinolate azo ligands. J Chem. Sci 2020;132:140-151.
30. Pearson RG. The principle of maximum hardness. A. Chem. Res 1993;26:250-255.
31. Rahmani R, Boukabcha N, Chouaih A. On the molecular structure, vibrational spectra, HOMO-LUMO, molecular electrostatic potential, UV–Vis, first-order hyperpolarizability, and thermodynamic investigations of 3-(4-chlorophenyl)-1-(1yridine-3-yl) prop-2-en-1- one by quantum chemistry calculation. J Mol. Struct 2018;1155:484-495.
32. Raynaud C, Norbert-Agaisse E, James B R, Eisenstein O. ^{31}P Chemical Shifts in Ru (II) Phosphine Complexes. A Computational Study of the Influence of the Coordination Sphere. Inorg. Chem 2020;59:17038-17048.
33. Reiffenstein RJ, Hulbert WC, Roth SH. Toxicology of Hydrogen Sulfide. Annu. Rev. Pharmacol. Toxicol 1992;32:109-134.
34. Scrocco E, Tomasi J. In P Lowdin (Ed) Advances in Quantum Chemistry. Academic Press, New York 1978.
35. Stone R, Marletta MA. Heme Stoichiometry of Heterodimeric Soluble Guanylate Cyclase. Biochem 1995;34:14668-14674.
36. Veber DF, Johnson SR, Cheng HY, Smith BR, Ward KW, Kopple KD. Molecular Properties That Influence the Oral Bioavailability of Drug Candidates J Med. Chem 2002;45:2615-2623.
37. Whiteman M, Armstrong JS, Chu SH, Ling SJ, Wong BS. The novel neuromodulator hydrogen sulfide: an endogenous peroxynitrite 'scavenger. J Neurochem 2004;90:765.
38. Zhao W, Zhang J, Lu Y, Wang R. The vasorelaxant effect of H2S as a novel endogenous gaseous KATP channel opener. EMBO J 2001;20:6008-6016.
39. Zoete V, Daina A, Bobigny C, Michielin O. Swiss Similarity: A Web Tool for Low to Ultra High Throughput Ligand-Based Virtual Screening. J Chem. Inf. Model 2016;56:1399-1404.